

# Evidence for scattering of curvature radiation in radio pulsar profiles

J. Dyks

*Nicolaus Copernicus Astronomical Center, Polish Academy of Sciences, Rabiańska 8, 87-100, Toruń, Poland*

Accepted .... Received ...; in original form 2020 Sep 22

## ABSTRACT

Radio pulsars exhibit several unexplained phenomena, in particular the average pulse profiles with the apparent core-cone structure and interesting frequency evolution. I show that they can be interpreted through essential geometric properties of the inverse Compton scattering. If the scattering occurs in a dipolar magnetosphere and the mean-free-path is long, a nested cone structure is expected with the cone size ratio of two-thirds, which is consistent with observations. Being a discontinuous process, the scattering is consistent with the discrete altitude structure of emission rings as derived from aberration-retardation effects. Assuming that the upscattered signal is the curvature radiation (CR), one can interpret the observed bifurcated components (BCs) as a magnified microbeam of CR: the BCs are wide low-frequency CR microbeams that have been upshifted in frequency with their width preserved by beam-copying scattering in divergent magnetic field. The large flux of BCs is partly caused by compression of the full emitted spectrum into the narrow observed bandwidth, which explains why the frequency-resolved BCs have the frequency-integrated shape. The wide low-frequency microbeams can encompass large magnetospheric volumes, which considerably abates the requirements of the energy needed for coherency. The properties of BCs thus suggest that the observed modulated radio flux is strongly affected by the scattering-driven blueshift and spectral compression. The relativistic beaming formula ( $1/\gamma$ ) is not always applicable, in the sense that it may not be directly applied to some blueshifted profile features.

**Key words:** pulsars: general – pulsars: individual: PSR J1012+5307 – pulsars: individual: PSR B1642–03 – pulsars: individual: PSR B1700–32 (PSR J1703–3241) – polarization – radiation mechanisms: non-thermal.

## 1 INTRODUCTION

Despite more than half a century of observations, and vast data collected for intensity profiles, polarization (Hankins & Rankin 2010; Stinebring et al. 1984; Noutsos et al. 2015; Tiburzi et al. 2013) and flux density modulation (Deshpande & Rankin 2001; Weltevrede et al. 2007), radiative pulsar properties resist most of interpretive efforts. The curvature radiation (CR) continues to be regarded as a likely emission process (Gangadhara 2010; Gil, Lyubarskii & Melikidze 2004; Luo & Melrose 1992; Mitra et al. 2009; Wang et al. 2015; Dyks et al. 2010, hereafter DRD10), despite it is not sufficiently energetic (Kaganovich & Lyubarsky 2010; Dyks & Rudak 2013) nor flexible enough to explain the observed signal geometry. The induced inverse Compton scattering (ICS) has been identified as the mechanism that likely reshapes the emitted radiation (Blandford & Scharlemann 1976; Lyubarskii & Petrova 1996). However, the scattering has been applied rather to extreme or peculiar phenomena (backward interpulses, non-bifurcated precursors, giant pulses, Petrova 2004, 2008a,b) and its role in shaping the regular profile morphology has not been recognized. In this paper I show that the regular pulsar profiles (main pulses) indeed bear a geometric signature of

scattering. Other arguments that are also based on the scattering allow us to make progress with the understanding of bifurcated emission components, such as those observed in PSR J1012+5307 (DRD10).

Average profiles of radio pulsars exhibit the mysterious nested cone morphology with the central component (core) surrounded by a pair or two pairs of conal components (Rankin 1983, 1993). Dipolar  $\vec{B}$  field offers little structure in the polar regions, therefore, since pulsar discovery in 1967, there has been only one interpretation proposed for the size ratio of the cones (Wright 2003). The present paper offers alternative view on the origin of the conal morphology in Section 2. In the following section some types of profile evolution with frequency are interpreted in terms of the scattering.

In Section 4 I discuss the origin of bifurcated components (BCs) observed in radio pulsar profiles. The excessive size of these components, and their similarity to the frequency-integrated CR microbeam will be both explained in a consistent way. Subsection 4.4 illustrates that the split part of the CR microbeam has the appropriate polarization to undergo efficient scattering.

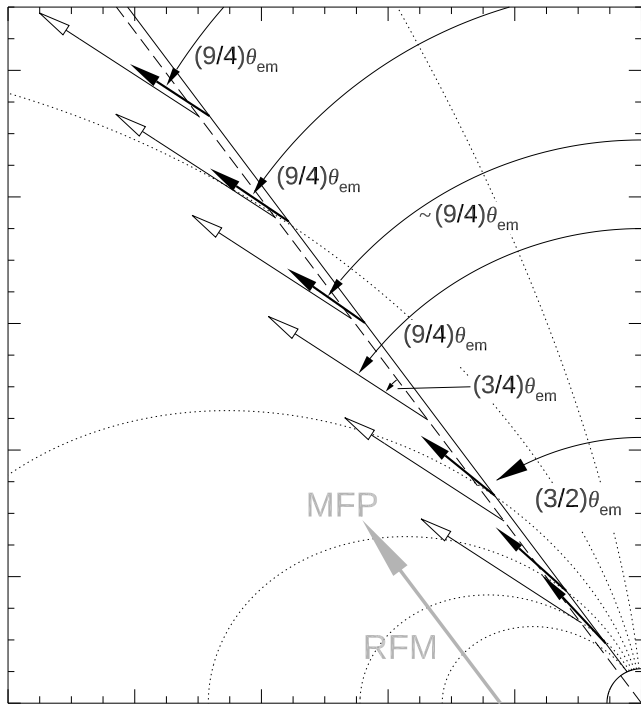


**Figure 1.** Formation of conal emission through scattering of low-altitude core rays that are emitted at  $(3/2)\theta_{\text{em}}$  and propagate upward along the near-diagonal solid line. The polar angle of the local  $B$ -field that they encounter (short black arrows) is quickly approaching  $(9/4)\theta_{\text{em}}$ . For any scattering altitude which is not close to the emission point, the emitted waves are scattered at this preferred angle, which produces a cone. White-tip arrows show the fixed local direction of  $\vec{B}$  along the dashed radial line which is parallel to the initial propagation direction. The low- $\nu$  profile widening is caused by the increase of the mean free path, as shown with the large grey arrow.

## 2 A MODEL FOR CONAL PROFILE MORPHOLOGY

The proposed scenario is based on key features of scattering in the relativistic limit: 1) the scattered photon is assumed to follow the electron's velocity, i.e. the local direction of magnetic field; 2) the scattered waves are blueshifted to a higher frequency, following the rough relation  $\nu_{\text{obs}} \sim \gamma^2 \nu_{\text{em}}$  between the scattered (observed) and emitted frequency.<sup>1</sup> I also assume the mean free path is sufficiently short for the efficient scattering to occur, where by efficient it is meant 'capable of producing a new pulse component'. Estimates of mean free path for nonisotropic scattering are sophisticated even with collective plasma effects ignored (eg. Dermer 1990; Dyks & Rudak 2000), but they are not necessary to make the geometric arguments of this paper. Existing estimates show that efficient scattering in pulsar polar tube is possible in the case of induced scattering (Blandford & Scharlemann 1976). Assuming that the incident radiation is amplified to the observed flux densities, Petrova (2008a) has shown that

<sup>1</sup> The neglected angular factor is expected to be important for small angle scatterings (photons following the electron within  $1/\gamma$ ) which can occur in pulsar magnetosphere, so this simplification should be released in a more exact analysis.

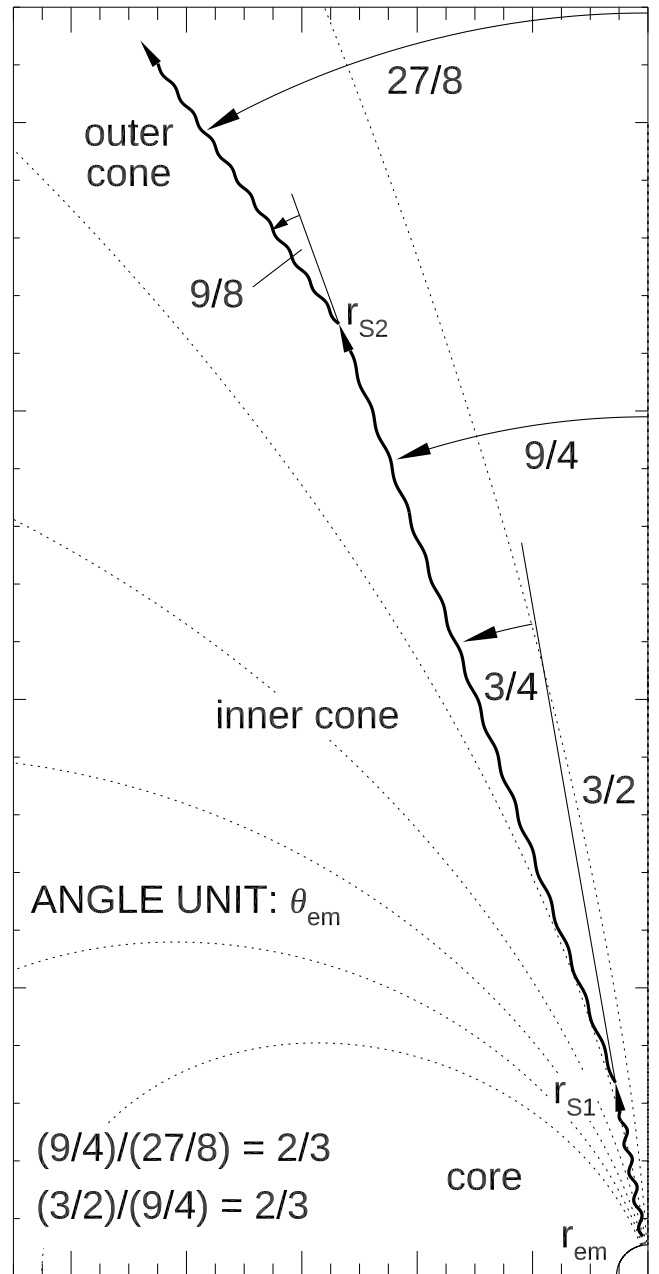


**Figure 2.** Relations between propagation angles in the core, inner cone and the outer cone rays. The unit of angle is the initial colatitude of an emission point  $\theta_{\text{em}}$  (arbitrary, but small). As explained in Fig. 1, the long mean free path and dipolar  $\vec{B}$  field ensure that beams of consecutive scattering orders are scaled by the factor of  $3/2$ . The inner to outer cone size ratio is thus equal to 0.66.

detectable precursors and interpulses can be formed in pulsar polar regions.

In the following it is argued that the cones correspond to the radiation that is scattered in the regime of a long mean free path (MFP), as suggested by the observed cone size ratio. Consider a low-altitude core ray emitted tangentially to the local magnetic field, at the polar angle  $(3/2)\theta_{\text{em}}$ , where  $\theta_{\text{em}}$  is the colatitude of the emission point, located at a radial distance  $r_{\text{em}}$ . The ray propagates along the solid slanted line in Fig. 1. In the relativistic limit, the ray will be scattered

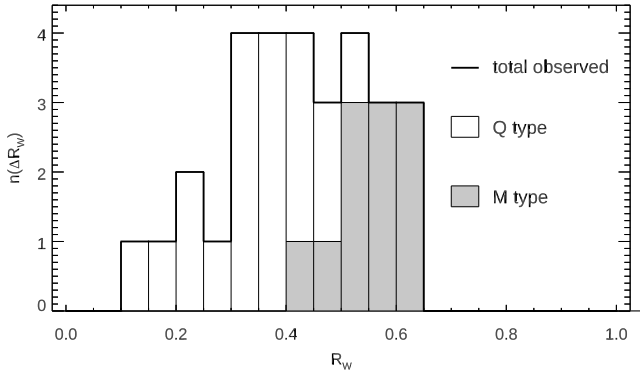


**Figure 3.** Histogram of component separation ratio ( $R_W = W_{\text{in}}/W_{\text{out}}$ ) for the inner and outer conal pair in quadruple and multiple profiles. After Dyks & Pierbattista (2015).

along the local  $\vec{B}$  field (black vectors) at a scattering angle  $\theta_{\text{sc}}$  as measured between the initial and scattered ray direction. The dipolar magnetic field along any radial line (including the dashed line parallel to the ray in Fig. 1) makes a fixed angle  $\theta_x$  with respect to the radial direction, as shown with the white tip arrows. The angle is equal to half the radial line tilt, in this case:  $\theta_x = (3/4)\theta_{\text{em}}$ . The corresponding polar angle (measured from the dipole axis) is equal to

$$\theta_{\text{obs}} = \frac{3}{2}\theta_{\text{em}} + \frac{3}{4}\theta_{\text{em}} = \frac{9}{4}\theta_{\text{em}}, \quad (1)$$

so it is larger by the factor  $3/2$  than the radial line tilt. Since the solid ray path is nearly radial far from  $r_{\text{em}}$ , the propagating ray is cutting the local  $\vec{B}$  field at an increasing angle which quickly approaches  $\theta_x$ . Only near the emission point, ie. for a short MFP (hereafter denoted  $\eta_{\text{sc}}$ ), the scattering direction depends on  $\eta_{\text{sc}}$  or altitude. For nonlocal scatterings ( $\eta_{\text{sc}} \gg r_{\text{em}}$ ) all the rays are scattered at the same polar angle  $(9/4)\theta_{\text{em}}$ . This can be interpreted as the inner cone.<sup>2</sup> The width ratio between the emitted and scattered beam is

$$R_{\text{io}} = \frac{3}{2}\theta_{\text{em}} \left( \frac{9}{4}\theta_{\text{em}} \right)^{-1} = \frac{2}{3}. \quad (2)$$

The above reasoning is recursive, so if the conditions allow for the second-order scatterings at long MFP, the outer cone is produced at the angle of  $(3/2)(9/4)\theta_{\text{em}} = (27/8)\theta_{\text{em}}$  (Fig. 2). The ratio of the inner to outer cone width is again  $R_{\text{io}} = 2/3 = 0.66$ .

The observed cone size ratio has been estimated in a nearly model-independent way from the measurements of the component separations in Q and M profiles (Dyks & Pierbattista 2015, hereafter DP15). In that method, the peak-to-peak separations  $W_{\text{in}}$  and  $W_{\text{out}}$  are measured for the inner and outer pair of conal components and the ratio  $R_W = W_{\text{in}}/W_{\text{out}}$  is calculated. The value of  $R_W$  only depends on the distance from the beam centre (called impact angle) at which the sightline is cutting the beam. The upper limit in the  $R_W$  distribution corresponds to the central sightline traverse through the beam (see fig. 1 in DP15) in which case we have

<sup>2</sup> Or the outer cone, if the emitted radiation is assumed to form a ring associated with the last open field lines. In that case, however, the core is an extra feature that needs explanation.

$R_W^{\text{max}} = R_{\text{io}}$ . As shown in Fig. 3 (after DP15, see also table 1 therein) ten percent of all the Q and M pulsars have the highest  $R_W$  value of 0.63 which is in good agreement with the scattering origin. The number of pulsars with near-maximum  $R_W$  is much lower than predicted for a conal structure, however, this can result from the beam suppression in the central-traverse region, as observed for the interpulse of PSR J1906+0746 (Desvignes et al. 2019).

Another known estimate of observed  $R_{\text{io}}$  is larger ( $\sim 0.75$ , Rankin 1993; Mitra & Deshpande 1999; Kramer et al. 1994), however, it was derived with indirect methods that use the curve of polarization angle (PA). As argued below (Section 3), the curve may be distorted by the scattering itself, and by other effects (eg. distortions that can be modelled as the coherent superposition of polarization modes, Dyks, Weltevrede & Ilie 2021).

Dipolar magnetic field geometry implies that for long  $\eta_{\text{sc}}$ , the scattering angle does not depend on scattering radii (Fig. 4, left) which must facilitate the appearance of the cones. Since all scattering angles are proportional to  $\theta_{\text{em}}$ , essentially the cones are reflected version of the core (Fig. 4, right). This is in line with the usually-similar width scale of observed core and cone components.

In the above-described version, the model assumes multiple scatterings. In a case with only a single scattering, a version of the model is possible in which the inner cone is formed by rays emitted near the last open lines (the emission is considered as the zeroth scattering order). The core in triple profiles can then be interpreted by a sightline grazing this inner (emitted) cone, whereas the scattered cone forms the single pair of conal components. Quadruple profiles (with four components) can also be interpreted in this model. However, in multiple-type profiles (with five components) the observed core component then requires a separate justification, see also Sect. 4.4.

### 3 FREQUENCY EVOLUTION OF PROFILES

The scattering model is in line with some types of observed frequency evolution of profiles. In particular, it is supported by profiles in which conal components emerge at high frequencies, as in PSR B1642–03 (Fig. 5 with frequency increasing downwards). This is consistent with the blueshifted nature of the scattered conal emission.

On the other hand, if the conditions are favorable, it is possible to observe well developed core and cones within the same frequency band. This is the case when the spectrum of the incident radiation (to be scattered) extends to sufficiently low frequency, or the blueshift is small on account of geometric effects. Fig. 6 shows the  $\nu$  evolution for PSR B1700–32, as observed by Parkes Telescope and GMRT (Johnston et al. 2008). To interpret such profile through scattering one must assume that the MFP decreases with increasing frequency (this assumption is the basis of the interpretation shown in Fig. 7). The upper part of Fig. 6 (GMRT, 243 and 322 MHz) suggests that below 243 MHz the profile is dominated by the core and likely follows the evolution which is observed in PSR B1642–03 (Fig. 5, cf. Fig. 7a,b).<sup>3</sup> The

<sup>3</sup> According to this view, the profiles of Figs. 5 and 6 represent different parts of a single scattering sequence shown in Fig. 7. The former set of profiles (for B1642–03) is continued in B1700–32.

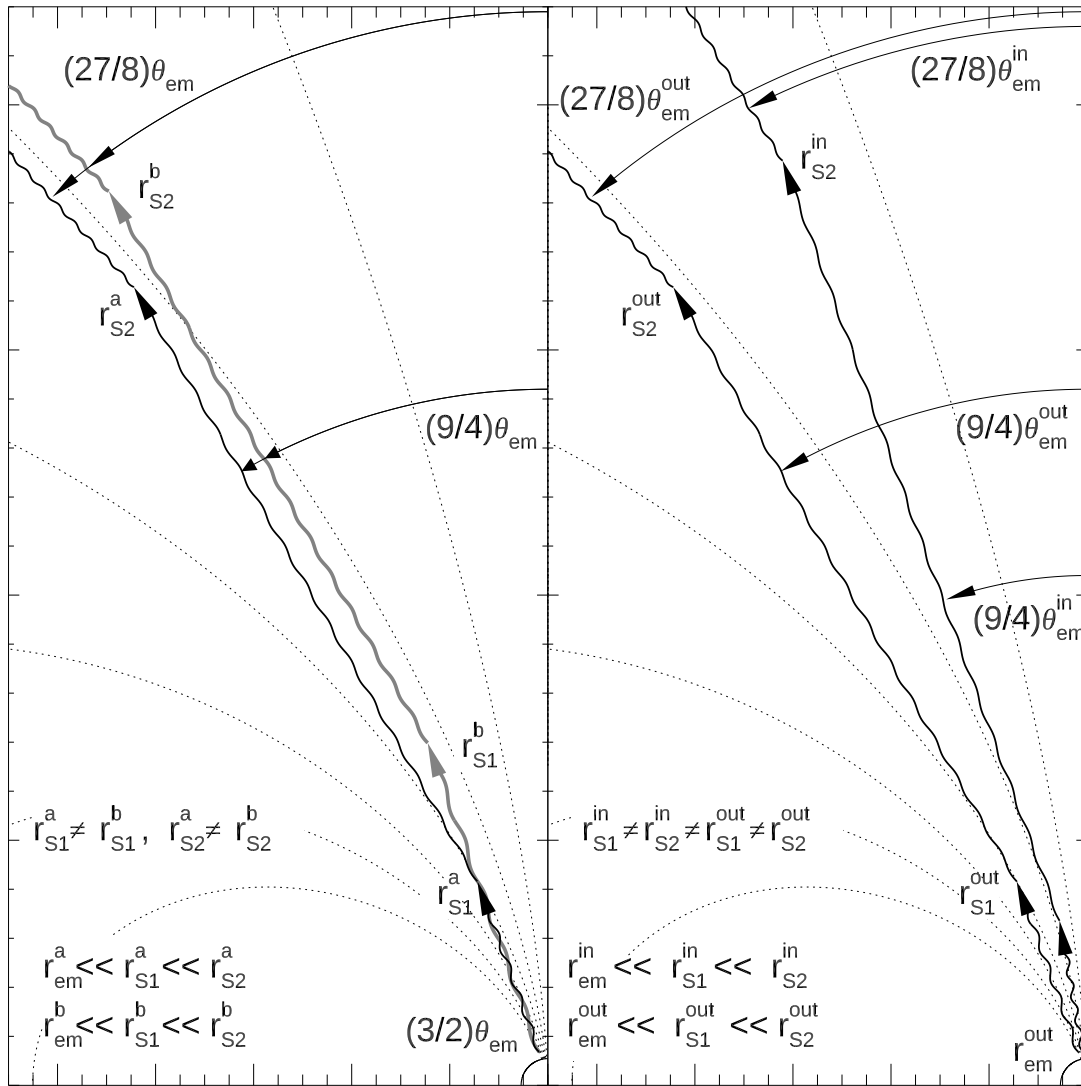


**Figure 4.** Geometry of long-MFP scattering for a pair of rays. Left: Two rays, ‘a’ (black) and ‘b’ (grey), emitted at the same polar angle  $(3/2)\theta_{em}$ . In spite of different scattering altitudes, the scattered rays of a given order propagate at the same polar angles, as shown with the double-tip arrows. Right: Two rays (inner and outer) emitted at different polar angles  $(3/2)\theta_{em}^{in}$  and  $(3/2)\theta_{em}^{out}$ . In each scattering order, the propagation directions of scattered rays preserve the initial angle ratio  $\theta_{em}^{in}/\theta_{em}^{out}$ .

blueshifted conals in Fig. 7a emerge at the unique distance from the core that corresponds to the long-MFP scattering angle (eq. 1). With increasing  $\nu_{obs}$  (and shorter MFP) the angles of scattering become smaller, because at lower altitudes the emitted photons cross the local  $\vec{B}$  at smaller angles (black arrows in Fig. 1). This makes the profile narrower. The triple form becomes less pronounced since the short MFP scatterings do not share the common scattering angle (which is only the feature of long-MFP scatterings). The pulse window is thus filled in with radio flux (Fig. 7b,c).

As shown in Fig. 7 (horizontal arrows), it is reasonable to expect that the transport of radio flux towards the profile periphery makes the PA curve flat. The outer parts thus do not have to correspond to the rotating vector model (RVM). The peripheric PA may consist of the ‘interior’ PA values

that have been relocated outwards by the scattering.<sup>4</sup> This effect is not accounted for in the usual PA modelling, which may explain the notorious problems with the RVM fitting of flat outer parts of PA curves (eg. PSR B1857–26, Mitra & Rankin 2008).

Since the scattering rate is different for different polarization modes, the cones are likely to have orthogonal polarization to that in the core, as it is often observed (eg. Srostlik & Rankin 2005). It is also the case for B1700–32: at 1.4 GHz the PA curve assumes a stairs-like shape, caused by the predominance of the other polarization mode in the core region. Despite the dominant OPMs swap in longitude, there is no trace of this in total polarization degree, which may be in-

<sup>4</sup> This intramagnetospheric PA flattening is different from the interstellar effect discussed in Karastergiou (2009).

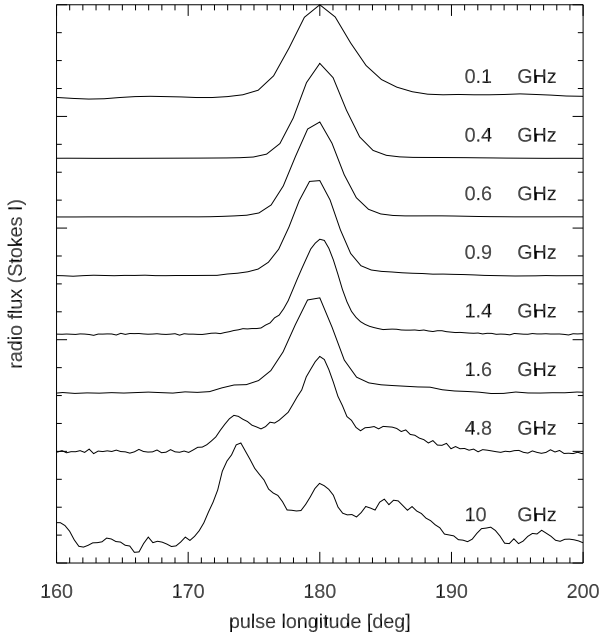


**Figure 5.** Average profiles of B1642–03 at eight frequencies that increase towards the figure’s bottom. Note the emergence of conal components above 1 GHz. Data from EPN (Gould & Lyne 1998; Seiradakis et al. 1995; von Hoensbroech & Xilouris 1997).

terpreted as a mostly-coherent orthogonal polarization mode jump (Dyks et al. 2021).

### 3.0.1 The radius-to-frequency mapping

The scattering geometry in dipolar  $\vec{B}$  field (Fig. 1) implies small scattering angles for short MFP. The small profile width at 3.1 GHz (bottom panels in Figs. 6 and 7) then corresponds to the local low-altitude scatterings that occur in the bottom right corner of Fig. 1. Thus, according to this model, the radius-to-frequency mapping (RFM) is caused by the changes of the scattering MFP. At high  $\nu_{\text{obs}}$  the short MFP is erasing the preference of the  $1.5\theta$  direction and fills in the polar tube, thus producing the narrow boxy profiles.

Pulsar profiles then seem to be shaped by the scattering-driven ray reflection. The cones in such model are produced at a higher altitude than the core, and the outer cones are located higher than the inner cones. This is what has been found observationally in the studies based on aberration-retardation effects (Gangadhara & Gupta 2001; Dyks et al. 2004; Krzeszowski et al. 2009). The core may also have different radio spectrum, because it must be mostly made of unscattered rays: since the scattering widens the incident beams, the narrowest beam likely corresponds to the unscattered (incident) radiation.

As discussed in Section 4.4, the core likely consists of the central (filled-in) part of the CR microbeam(s), which has the unfavourable polarization orientation of the extraordinary mode, thus avoiding the scattering. Unlike that, the split O-mode part of the beam is widened into cones (deflected outwards by scatterings). When at high frequency the scattering ceases to deflect the O-mode outwards, both polarization modes are observed together within the narrow core-

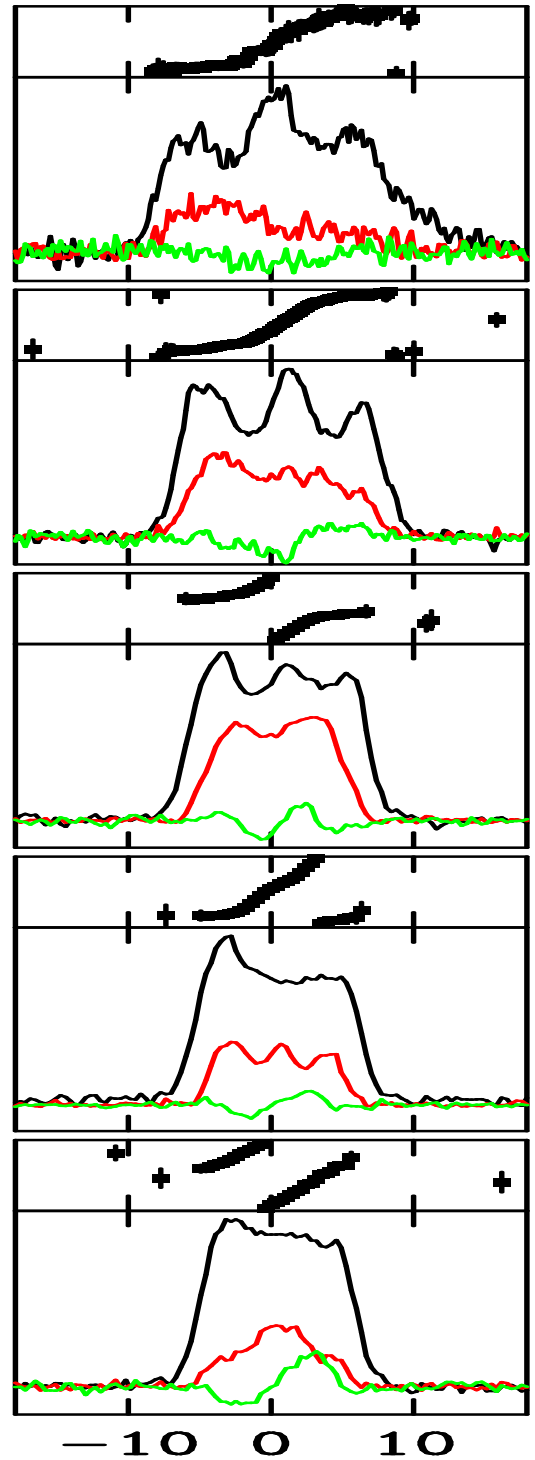


**Figure 6.** Frequency evolution of the polarized profile of PSR B1700-32 (fig. 4 in Johnston et al. 2008). From top to bottom, the frequencies are: 243 and 322 MHz (GMRT) and 0.69, 1.4 and 3.1 GHz (Parkes Telescope). The range of PA axis is  $(-90^\circ, 90^\circ)$ , the longitude is in degrees. Note the stairs-shaped PA at 1.4 GHz, and the emergence of conals with flat PA.

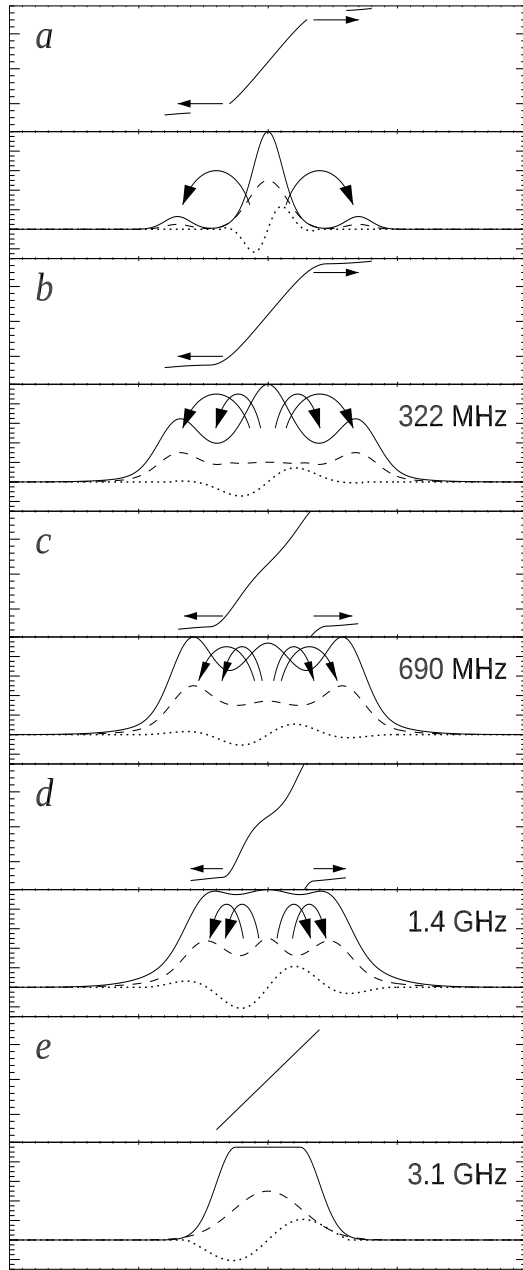


**Figure 7.** Schematic interpretation of the frequency evolution observed in PSR B1700-32 (Fig. 6). Bent arrows show the ray displacement by the scattering. Horizontal arrows show the associated PA displacement, which may lead to the flattening of the peripheral PA curves. Top two panels reflect the behaviour of B1642-03 (Fig. 5).

like boxy profile. This implies depolarization which is indeed often observed at high  $\nu$  (eg. Noutsos et al. 2015; also see Fig. 6 in this paper).<sup>5</sup>

<sup>5</sup> Refraction would imply similar mode-dependent effects, however, refraction does not imply specific cone size ratio. Still, I do not exclude a possible contribution of refraction at the lowest observed frequencies (few hundreds of MHz).

#### 4 THE NATURE OF BIFURCATED COMPONENTS

The bifurcated components (BCs) can be divided in two classes: narrow conal components that merge quickly with increasing frequency ( $\Delta \propto \nu^{-1/2}$ , see fig. 6 in Dyks et al. 2007) and do not resemble the CR microbeam shape. A typical example is the trailing conal component in the millisecond PSR J0437-4715 (Navarro et al. 1997; Dai et al. 2015; Osłowski et al. 2014) although conal BCs have also been observed in normal pulsars (PSR B1946+35, Mitra & Rankin (2017), B1933+16 Mitra et al. 2016).<sup>6</sup> The other BCs are very wide precursors – the primary example is the strong and very symmetric interpulse precursor in PSR J1012+5307 (Fig. 8, based on fig. 8 in DRD10). The peaks in this BC merge with  $\nu$  at the rate  $\Delta \propto \nu^{-0.35}$  which is close to that of the CR microbeam ( $\Delta \propto \nu^{-1/3}$ ). The BC has a shape that is similar to the  $\nu$ -integrated CR microbeam.

It is suggested here that the two BC types correspond to two different scattering regimes. The narrow fast-merging BCs are scattered within a magnetospheric region with small spread of velocity directions:  $\Delta \hat{v} \ll 1/\gamma_{sc}$ , where the hat means a unit vector, and  $\gamma_{sc}$  is the Lorentz factor of the scattering electrons. With no widening by the velocity spread, this implies the scattered beam size  $\Delta \sim 1/\gamma_{sc}$ . In the case of ICS, the observed frequency is roughly equal to  $\nu_{obs} \approx \gamma_{sc}^2 \nu_{em}$ , where  $\nu_{em}$  represents the peak frequency of the emitted CR spectrum. Hence  $\Delta \propto (\nu_{em}/\nu_{obs})^{1/2}$ , ie. the  $\nu$ -dependence of these BCs is directly consistent with the ICS origin (Dyks et al. 2007).

The strong BC in PSR J1012+5307 merges with  $\nu$  at the rate expected for CR. However, although it has been observed within a narrow frequency band of 8%, it has a shape that is very similar to the  $\nu$ -integrated CR microbeam (Fig. 8). In the  $\nu$ -resolved microbeam the intensity of CR drops steeply in the periphery (at a super-Gaussian rate, ie. the dotted line in Fig. 8 follows eq. 4 in DRD10), whereas the  $\nu$ -integrated microbeam has well-developed wings, which extend far outwards (eq. 8 in DRD10).<sup>7</sup> The observed  $\nu$ -resolved BC should therefore be strongly dissimilar to the  $\nu$ -integrated CR microbeam that is fitted in Fig. 8 (solid line). Instead, the  $\nu$ -integrated CR beam produces a decent fit: between the dashed vertical lines  $\chi^2/\text{dof} = 3.6$  (DRD10). The strong outer wings cannot be explained by spatial convolution, because it would mostly fill in the central minimum in the observed BC (fig. 3 in Dyks & Rudak 2013). Moreover, the BC is about ten times wider than the CR microbeam, which has the peak separation of  $\Delta_{cr} \approx 0.8^\circ / (\nu^{1/3} \rho_{B,7}^{1/3} \sin \delta_{cut} \sin \zeta)$ , where  $\rho_B = 10^7 \text{ cm} \rho_{B,7}$  is the curvature radius of electron trajectory,  $\delta_{cut}$  is the angle at which the sightline crosses the split fan beam, and  $\zeta$  is the viewing angle between the sightline and the pulsar rotation axis (see fig. 2 in Dyks et al. 2012).

##### 4.1 Doppler magnification

The two problems (the large width and the forbidden similarity of the  $\nu$ -resolved to the  $\nu$ -integrated beam) become

<sup>6</sup> The bifurcations are illustrated, but not mentioned in the cited papers.

<sup>7</sup> The analytical formulae for the shapes of both  $\nu$ -resolved and  $\nu$ -integrated beams are provided in Section 4.4.

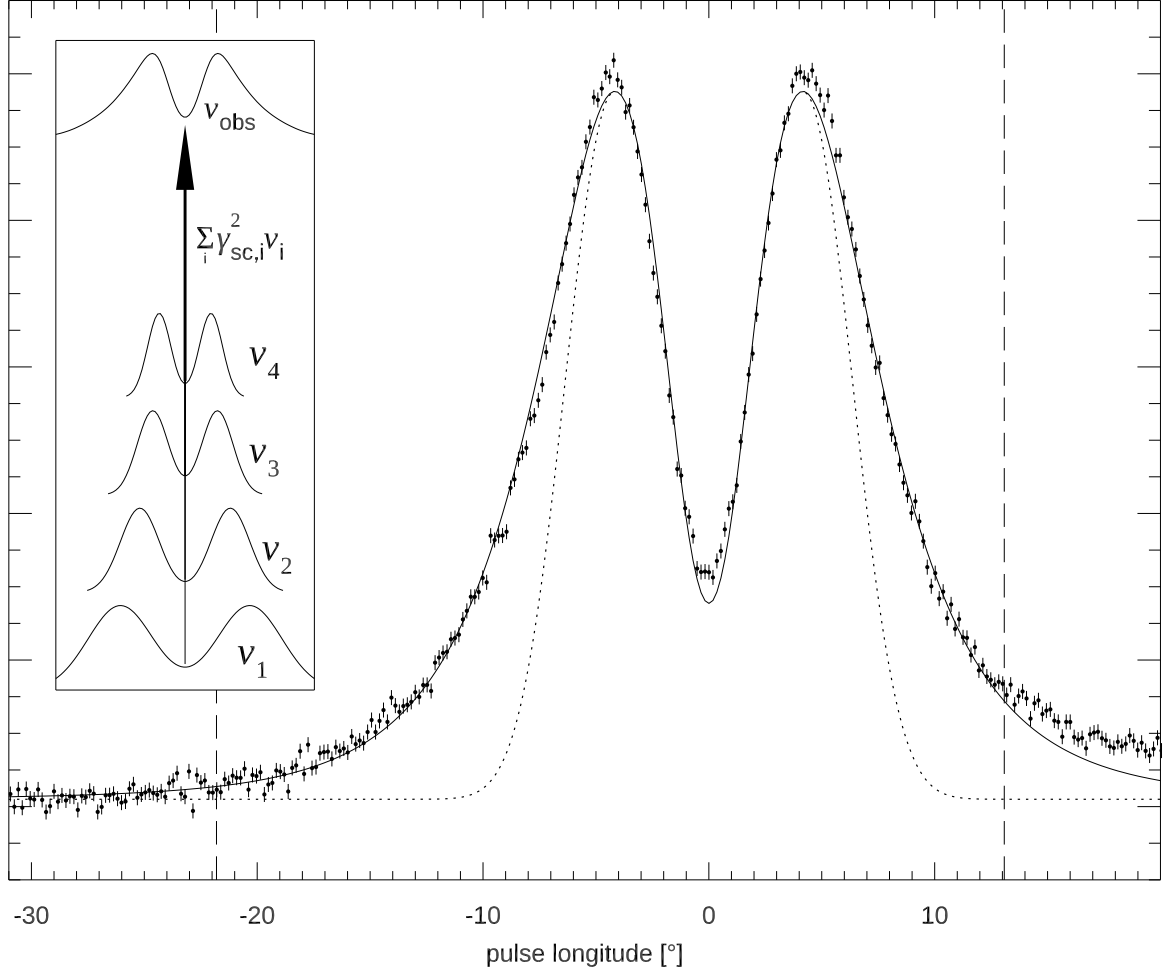


**Figure 8.** The BC in PSR J1012+5307, as observed at 0.82 GHz by GBT (from Dyks et al. 2010). In spite of the narrow bandwidth of 64 MHz (8%) the BC is well modelled by the  $\nu$ -integrated O-mode-dominated CR beam (within the dashed verticals  $\chi^2/\text{dof} = 3.6$ , error bars are statistical  $1\sigma$ , vertical scale in arbitrary units). Dotted line shows the steep outer wings in the frequency-resolved CR beam. Inset: the bright outer wings are formed by Doppler-stacking (through blueshifting) of wide low- $\nu$  CR microbeams: waves of different  $\nu$  are scattered by electrons with different energy  $\gamma_{sc}$ . The large size of the low- $\nu$  microbeams is preserved by the beam-copying scattering (see next figure).

solved and consistent with each other as soon as the BC originates from scattering in the regime of large spread of velocity directions ( $\Delta\hat{v} \gg 1/\gamma_{sc}$ ) and non-negligible spread of scattering electron energies ( $\gamma_{sc}$ ). If the wide low- $\nu$  CR microbeam is scattered in a region with diverging  $\vec{B}$  field (grey rectangle in Fig. 9), then each ray is directed along the black vectors of the local  $\vec{B}$ -field. Although the aberration works as usual in this scattering (sending a ray along the electron velocity), the entire original CR microbeam is not collimated (relativistically beamed) because different parts of the CR microbeam (different rays) are scattered at different magnetospheric locations by electrons moving in different directions (nonlocal scattering). The beam size and shape is thus copied (ray by ray) from the low  $\nu$  to the high observed frequency  $\nu_{\text{obs}} \approx \gamma_{sc}^2 \nu$ . The spread of  $\vec{B}$  can slightly magnify the beam (by less than 3/2, as shown in Fig. 9), however, the key magnification comes from the translation in the frequency space. The beam essentially does not become wider – it is just made wider than expected at the observed  $\nu_{\text{obs}}$ , but roughly of the

same size as at the much lower  $\nu$  before the scattering (see inset in Fig. 8).

#### 4.2 Spectral compression

The second property – similarity to the  $\nu$ -integrated microbeam, results from the spread of the scattering electron energy. Following the gamma-square rule  $\nu_{\text{obs}} \approx \gamma_{sc}^2 \nu$ , higher-energy electrons pick up lower frequencies from the emitted CR spectrum, and deposit the flux at the same  $\nu_{\text{obs}}$ . The lower- $\nu$  CR is emitted in wider microbeams, which contribute predominantly to the outer wings of the observed high- $\nu$  BC. All the different CR microbeams in the emitted CR spectrum join the narrow observed band, and make the BC look  $\nu$ -integrated. Thus, the  $\nu$ -integrated shape results from the convolution of the electron energy distribution with the emitted CR spectrum (the high- $\nu_{\text{obs}}$  profile in the inset of Fig. 8 is the sum of the four inset profiles shown below).

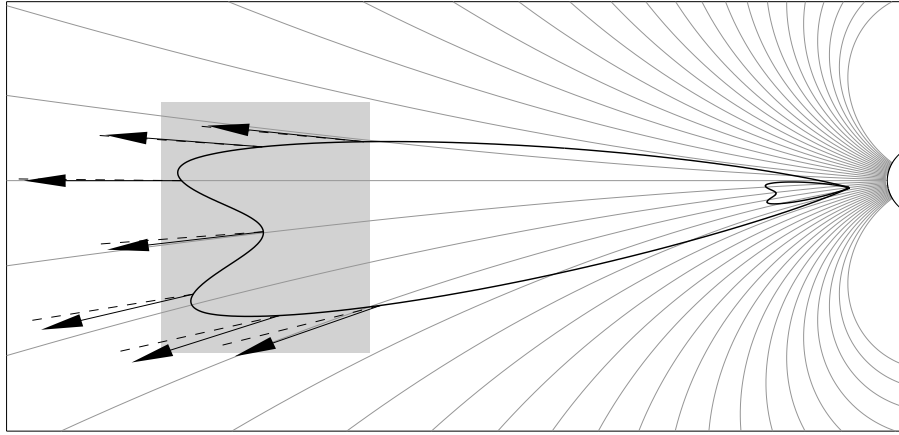


**Figure 9.** The mechanism of the ray-to-ray beam copying by scattering. Individual rays in the emitted beam (propagating along the dashed lines) are locally scattered along the black arrows that represent the local velocity direction for distant electrons. The wide low- $\nu$  beam shape is thus copied to the high  $\nu_{\text{obs}}$  with its large width approximately preserved. Unlike the B-field lines, the dashed rays are located within the page plane. The rays cross the local  $\vec{B}$  at an angle larger than  $1/\gamma_{\text{sc}}$  because  $\vec{B}$  within the grey rectangle is penetrating the page at some angle ( $\sim \theta_x$ ), so that the side view resembles Fig. 1.

### 4.3 Electron energies and energy budget

The BC of J1012+5307 has the 1-GHz width of about  $8^\circ$  but it may be enlarged by oblique sightline cut (small  $\delta_{\text{cut}}$ ) by unknown factor. Assuming 0.1 rad for its real width, the electrons have the Lorentz factor of  $\gamma_{\text{em}} \sim 10$ , and emit very low-frequency CR at  $\nu_{\text{cr}} \approx 7$  GHz  $\gamma_{\text{em}}^3/(\rho_B[\text{cm}]) \sim 1$  MHz. To reach the observed GHz band, the scattering electrons must have  $\gamma_{\text{sc}} \sim 30$ . This is pretty close to  $\gamma_{\text{em}} \sim 10$ , which suggests the same energy distribution for both the emitting and scattering electrons. The mechanism can thus be called the curvature-self-Compton radiation.

The ten-fold increase of beam size implies that the energy budget problem is abated by three orders of magnitude on account of the increased volume alone. Furthermore, the energy available within the radio band is no longer restricted by the spectral properties of the CR, since the observed BC is mostly powered by the scattering electrons. In the case of the BC of J1012+5307 the required efficiency of energy transfer to the radio band has been previously estimated as  $10^{-4}$  of the maximum power of a plasma stream, as limited by the electric potential drop and possible stream width (Dyks & Rudak 2013). Since this estimate is proportional to the stream cross-section  $A$  (see eq. 3 therein), the tenfold increase of microbeam size decreases this power transfer efficiency to  $10^{-6}$ .

### 4.4 Does the split beam have the right polarization to be scattered?

Blandford and Scharlemann (1976) have shown that only the ordinary polarization mode is efficiently scattered in strong magnetic field. The mode is polarized in the plane that contains the wave vector  $\vec{k}$  and the local magnetic field  $\vec{B}$ . The split part of the curvature radiation beam is known to be polarized across the plane of a B-field line. Superficially, this may lead us to erroneously think that the split part of the beam may not be scattered, which is not the case. This point is sometimes overlooked, so it will be discussed explicitly in the following.

Fig. 10 schematically shows the curvature radiation beam emitted by an electron moving along the curved magnetic field line (dashed line). The customary derivation of the beam's intensity results in the well known formula consisting of two terms:

$$I_{\text{cr}} = f_1 + f_2 \sin^2 \psi \quad (3)$$

where  $\psi$  is the angle between  $\vec{k}$  and  $\vec{B}$ .<sup>8</sup> The first term represents the filled-in part of the beam (grey lobe in Fig. 10), which is polarized along the electron acceleration vector  $\vec{a}$  (the polarization direction is shown with the short double-tip arrows). The second term (psi-squared term) corresponds to the split part of the beam (black solid lobes in Fig. 10) which is polarized along  $\vec{k} \times \vec{a}$ , where  $\vec{k}$  is the wave vector pointing towards the observer. The angle  $\psi$  is exaggerated in the figure, because even at a very low frequency ( $\sim 1$  MHz) the CR beam has the opening angle around 0.1 rad. Therefore, the polarization of the split beam is approximately orthogonal to the B-field line plane. However, in spite of such almost orthogonal orientation, the polarization is within the  $\vec{k}$ - $\vec{B}$  plane. Thus, it is the split part of the curvature beam that has the polarization of the ordinary mode.<sup>9</sup> Therefore, contrary to the initial pessimistic suspicion, the split fan beam of the curvature radiation has the polarization favorable for the scattering.<sup>10</sup>

<sup>8</sup> The form of  $f_1$  and  $f_2$  is given below in eq. (5) but it is not important for the present discussion.

<sup>9</sup> Whereas the central filled-in part, which is polarized parallel to the B-line plane, is polarized in the direction of the X mode.

<sup>10</sup> The polarization of the beam parts with respect to the B-field line plane (parallel/orthogonal) is described by adjectives that must be replaced with each other as soon as the reference to the propagation modes is made (parallel/orthogonal beam parts correspond to orthogonal/parallel polarization of modes). In DRD10 the B-line-based polarization of beam parts has been directly extended to the names of the polarization modes which is incorrect (hence the names 'X mode' and 'O mode' should be replaced with each other, and similarly the symbols  $\parallel$  and  $\perp$ ). The mode-related designation of intensity terms (indices  $\parallel$  and  $\perp$ ) is used eg. in Ry-



#### 4.4.1 The question of the core component

With the X mode polarization, the central microbeam part (or a spatially convolved bundle of such beam parts) is likely to represent the undeflected (not widened) central part of the profile, ie. the core. The core component has indeed been shown to have the low-altitude opening angle of the polar tube (Rankin 1990).

#### 4.5 Wings of the classical curvature radiation beam

Following the remarks of Section 4.4, we may write down the CR beam formula using the indices  $\perp$  and  $\parallel$  with reference to the  $\vec{k} \times \vec{a}$  plane (hence appropriate to the modes). The energy emitted per unit solid angle and unit frequency is:

$$\begin{aligned} \eta_{\text{cr}} &= \eta_{\perp} + \eta_{\parallel} = \\ &= \frac{q^2 \omega^2}{3\pi^2 c} \left(\frac{\rho}{c}\right)^2 \left[ \xi^2 K_{2/3}^2(y) + \xi K_{1/3}^2(y) \sin^2 \psi \right], \end{aligned} \quad (4)$$

where

$$\xi = 1/\gamma^2 + \psi^2, \quad \text{and} \quad (6)$$

$$y = \frac{\omega \rho}{3c} \xi^{3/2}. \quad (7)$$

Here  $\rho$  is the radius of curvature of electron trajectory,  $\omega = 2\pi\nu$ ,  $c$  is the speed of light, and  $K$ 's are the modified Bessel functions. The angle  $\psi$  is measured from the plane of the electron trajectory (Fig. 10).

Using the lowest term in the large-argument expansion of the modified Bessel functions (Abramowitz & Stegun 1972):

$$K_{2/3}(y) \simeq K_{1/3}(y) \simeq \left(\frac{\pi}{2y}\right)^{1/2} e^{-y} \quad (8)$$

the shape of the outer wings ( $\psi > 1/\gamma$ ) becomes:

$$\eta_{\text{cr}}(\text{wings}) \simeq \frac{q^2 \nu \rho}{c^2} |\psi| e^{-|\psi|^3/\sigma_{\text{cr}}^3} \left(1 + \frac{\sin^2 \psi}{\psi^2}\right) \quad (9)$$

where we introduce a parameter  $\sigma_{\text{cr}} = (3c/(2\omega\rho))^{1/3}$ . Ignoring the difference between  $\sin \psi$  and  $\psi$  it is found that wings of both modes have equal strength and the same 'super-Gaussian' shape of type  $|\psi| \exp(-a|\psi|^3)$ . The wings are shown as dotted line in Fig. 8).

In the  $\nu$ -integrated case the CR beam represents the power emitted per steradian:

$$\begin{aligned} I_{\text{cr}} &= I_{\perp} + I_{\parallel} = \frac{7q^2 c}{256\pi \rho^2} \left(\frac{2\beta^7}{\cos \psi}\right)^{1/2} \times \\ &\times (1 - \beta \cos \psi)^{-5/2} \left(1 + \frac{5}{14} \frac{\beta \cos \psi \sin^2 \psi}{1 - \beta \cos \psi}\right), \end{aligned} \quad (10)$$

where  $\beta$  is the electron velocity in units of  $c$ . Since  $1 - \beta \cos \psi \simeq \psi^2/2$ , both modes have wings of type  $(1 - \beta \cos \psi)^{-5/2} \propto \psi^{-5}$  (cf. eq. 12 in DRD10).

Depending on how large part of the CR spectrum has been integrated within the observed bandwidth (or has been stacked there by the scattering) the shape of a component

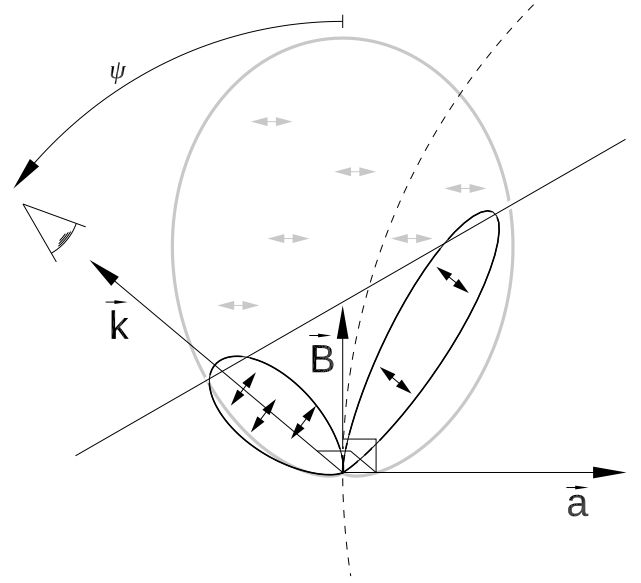


**Figure 10.** Customary decomposition of the curvature radiation beam in two orthogonally polarized parts: the part peaking along  $\vec{B}$  (grey) is polarized along the acceleration  $\vec{a}$  whereas the bifurcated part (black solid) is polarized orthogonally to the plane containing  $\vec{k}$  and  $\vec{a}$ . The latter polarization is in the plane of  $\vec{k}$  and  $\vec{B}$  which is the polarization of the ordinary mode. The dashed line is the curved electron trajectory.

may be closer to the limit (9) or (11). Additionally, a convolution with the spatial emissivity distribution may be needed.<sup>11</sup> Some contribution from the spatial extent likely affects the BC in Fig. 8. The central flux in the model shown with the solid line is fully provided by the filled-in X-mode part of the beam (normalized first term of eq. 11) which likely plays the role of the spatial extent.

## 5 DISCUSSION

### 5.1 Implications for subpulse modulations

The properties of bifurcated components imply that spectral effects play crucial role in determining the observed flux of single pulse radio emission. First, the scattering must blueshift the emitted radio spectrum to reach the high frequency band normally used by radio telescopes. Second, the flux is further amplified by compressing the emitted spectrum into the narrow bandwidth used in the observations. From the observational point of view, where flux modulations by a factor of a few make a noticeable difference, the scattering looks like a crucial flux-determining factor.

When the modulation phenomena are attributed to the spectral variations, it seems natural that many of them do not involve displacement of subpulses in pulse longitude. It appears that the temporal variations of the electron energy spectrum (hence of the observed radio flux and spectrum) are at least as important for the flux modulations as the lateral rotation from the ExB drift.

bicki & Lightman (1979, eq. 6.29), whereas Jackson (1975) uses the indexing based on the B-field line plane.

<sup>11</sup> This discussion assumes that the beam is not deformed by the process that makes it coherent.

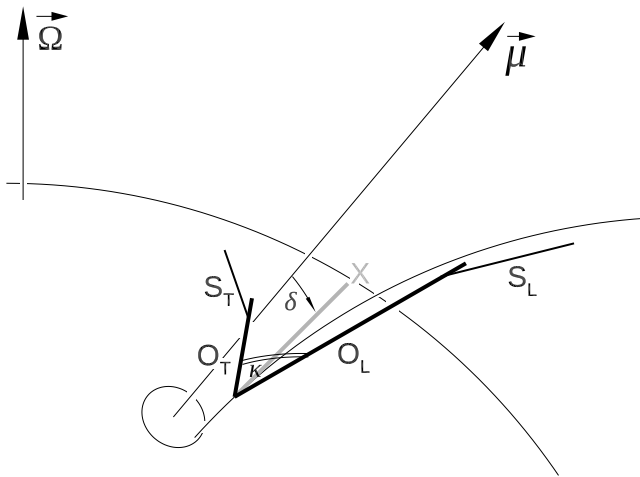


**Figure 11.** Geometry of the low-altitude fan-beam emission from a bent plasma stream (the arc emerging from the polar cap). Sections  $O_T$ ,  $X$ , and  $O_L$  represent the axes of the CR beam parts shown in Fig. 10. When the beam’s opening angle  $\kappa$  is larger than the beam’s tilt  $\delta$ , the O-mode rays  $O_T$  and  $O_L$  roughly follow the geometry of Fig. 1 with the scattered rays  $S_T$  and  $S_L$  following similar beam size ratio  $W_O/W_S \approx 2/3$ .

## 5.2 Cones or fan beams?

The presented model is clearly ambivalent with respect to the conal-or-fan beam alternative.

Section 1 suggests the concentric rings (nested conal beams) whereas the BCs are interpreted as cuts of sightline through the split-fan beams. It does not help to say that conal components are different than the bifurcated precursors observed in J1012+5307, because the bifurcations are also observed in the normal conal components of the pulsars mentioned at the beginning of Section 4. The bifurcations have been considered as the main justification for the non-conal beam geometry (system of radial fan beams, see fig. 18 in DRD10), because the diverging plasma flow in the polar region is expected to smear any structure in magnetic latitude (fig. 1 in Dyks 2017a). One possibility is to claim that conal components in different pulsars may have different origins: they are either deflected (scattered) rays from the ring-shaped emission regions, or they result from a cut through the fan beam emission from a bent ‘conal’ stream (a stream lying not in the main meridian).

Another option is to assume that only the fan beams exist (instead of rings or cones). The system of fan beams is known to exhibit the same RFM and aberration-retardation effects as the conal region (Karastergiou & Johnston 2007; Dyks et al. 2015) and has favorable statistical properties (Lyne & Manchester 1988; Chen & Wang 2014). By allowing for the wide microbeams, one may also consider a version of the fan beam model with the pulse structure formed by the microbeam shape, instead by the flow structure. In such microbeam-based fan beam model the scattering can produce a doubly-split fan beam as shown in Fig. 11 (with the core formed by the unscattered central X mode). The four-component profile of J0631+1036 may be interpreted as a doubly-split (four-lobed) fan beam structure on account of problems described in section 3 of Teixeira et al. (2016). In fact, by assuming that the microbeam opening angle  $\kappa$

is larger than the beam’s tilt  $\delta$  with respect to the dipole axis, it is possible to derive the same ‘conal’ size ratio of 2/3 (Fig. 11). This is because for  $\delta \sim 0$ , the O-mode rays  $O_T$  and  $O_L$  propagate essentially in the same way as shown in Fig. 1. However, the ratio of 2/3 seems to be a lower limit in the case of such microbeam-based doubly-split fan beam, which then likely does not reproduce the distribution of Fig. 3.<sup>12</sup> For this reason it is the mixed scenario (involving the cones and fan beams) that appears to be the most likely possibility. Whereas the scatterings can explain the apparent conal properties, they do not necessarily prove that the geometry behind all conal components is conal.

## 6 CONCLUSIONS

It has been shown that the general properties of the inverse Compton scattering can explain the apparent nested cone geometry with the observed conal size ratio. The blueshift of the scattered radiation is consistent with some types of frequency evolution of profiles, in particular with the emergence of conal components at high  $\nu$ . The scattering is also consistent with discreteness of the invoked polar emission rings (cones), as well as with their altitude structure as derived from the aberration-retardation effect (higher altitude of outer rings).

Assuming that the incident waves are the curvature radiation, it is also possible to understand the peculiar properties of bifurcated components. This includes their rate of merging, their flat outer wings, and their oversized dimensions. The width-saving transportation of the emitted CR beam up to a much higher observed frequency must be responsible for the large size of BCs. This implies that the relativistic beaming formula ( $\Delta \sim 1/\gamma$ ) does not always hold, in the sense that it may not be directly applied to the width of the Doppler-magnified components in pulsar profiles. Moreover, the low- $\nu$  microbeams (to be scattered) have angular sizes comparable to the entire polar tube, which decreases the energy requirements for generation of coherency.

It is also concluded that both the shape of components in average radio pulse profiles, and the observed signal modulations are strongly affected by processes that occur in the frequency space. In particular, the outer wings of components are very sensitive to the effect of spectral stacking of flux within the observed narrow frequency band. The modulation properties depend on whether the scattered spectrum includes the observed band, which depends on details of scattering geometry and plasma flow structure.

This paper solves the main obstacles in our previous papers on BCs (the problem of large width and the  $\nu$ -integrated shape). It has been emphasized now that the orthogonal-to-fieldline polarization of the split part of the curvature beam is actually consistent with the orientation of the ordinary

<sup>12</sup> Moreover, if a conal component comes from the scattering of a single O-mode lobe (say  $O_T$  into  $S_T$ ) we must again explain why  $S_T$  would be sometimes observed as bifurcated. One would have to argue that the scattered rays  $S_T$  and  $S_L$  activate CR emission of new streams which themselves emit bifurcated microbeams. This would lead to a branching stream with causally connected branches and interesting modulation properties.

mode waves, which is parallel to the  $\vec{k}$ - $\vec{B}$  plane (and this polarization mode is expected to be scattered efficiently). This paper then offers a self-consistent scenario providing further credence to the idea, that resolved and magnified views of microscopic radiation patterns are made visible to us by pulsars.

## ACKNOWLEDGMENTS

I thank Simon Johnston for Fig. 2. This work was supported by the grant 2017/25/B/ST9/00385 of the National Science Centre, Poland.

## DATA AVAILABILITY STATEMENT

This paper is based on published data.

## REFERENCES

- Abramowitz M., Stegun I. A., 1972, Handbook of Mathematical Functions
- Blandford R. D., Scharlemann E. T., 1976, MNRAS, 174, 59
- Chen J. L., Wang H. G., 2014, ApJS, 215, 11
- Dai S., Hobbs G., Manchester R. N., Kerr M., Shannon R. M., van Straten W., Mata A., Bailes M., Bhat N. D. R., et al., 2015, MNRAS, 449, 3223
- Dermer C. D., 1990, ApJ, 360, 197
- Deshpande A. A., Rankin J. M., 2001, MNRAS, 322, 438
- Desvignes G., Kramer M., Lee K., van Leeuwen J., Stairs I., Jessner A., Cognard I., Kasian L., Lyne A., Stappers B. W., 2019, Science, 365, 1013
- Dyks J., 2017, MNRAS, 471, L131
- Dyks J., Pierbattista M., 2015, MNRAS, 454, 2216
- Dyks J., Rudak B., 2000, A&A, 360, 263
- Dyks J., Rudak B., 2012, MNRAS, 420, 3403 (DR12)
- Dyks J., Rudak B., 2013, MNRAS, 434, 3061
- Dyks J., Rudak B., 2015, MNRAS, 446, 2505
- Dyks J., Rudak B., Demorest P., 2010, MNRAS, 401, 1781 (DRD10)
- Dyks J., Rudak B., Harding A. K., 2004, ApJ, 607, 939
- Dyks J., Rudak B., Rankin J. M., 2007, A&A, 465, 981
- Dyks J., Weltevrede P., Ilie C., 2021, MNRAS, 501, 2156 (DWI21)
- Gangadhara R. T., 2010, ApJ, 710, 29
- Gangadhara R. T., Gupta Y., 2001, ApJ, 555, 31
- Gil J., Lyubarsky Y., Melikidze G. I., 2004, ApJ, 600, 872
- Gould D. M., Lyne A. G., 1998, MNRAS, 301, 235
- Hankins T. H., Rankin J. M., 2010, AJ, 139, 168
- Jackson J. D., 1975, Classical electrodynamics
- Johnston S., Karastergiou A., Mitra D., Gupta Y., 2008, MNRAS, 388, 261
- Kaganovich A., Lyubarsky Y., 2010, ApJ, 721, 1164
- Karastergiou A., 2009, MNRAS, 392, L60
- Karastergiou A., Johnston S., 2007, MNRAS, 380, 1678
- Kramer M., Wielebinski R., Jessner A., Gil J. A., Seiradakis J. H., 1994, A&AS, 107, 515
- Krzyszowski K., Mitra D., Gupta Y., Kijak J., Gil J., Acharyya A., 2009, MNRAS, 393, 1617
- Luo Q., Melrose D. B., 1992, MNRAS, 258, 616
- Lyne A. G., Manchester R. N., 1988, MNRAS, 234, 477
- Lyubarskii Y. E., Petrova S. A., 1996, Astronomy Letters, 22, 399
- Mitra D., Deshpande A. A., 1999, A&A, 346, 906
- Mitra D., Gil J., Melikidze G. I., 2009, ApJ, 696, L141
- Mitra D., Rankin J., 2017, MNRAS, 468, 4601
- Mitra D., Rankin J., Arjunwadkar M., 2016, MNRAS, 460, 3063
- Mitra D., Rankin J. M., 2008, MNRAS, 385, 606
- Navarro J., Manchester R. N., Sandhu J. S., Kulkarni S. R., Bailes M., 1997, ApJ, 486, 1019
- Noutsos A., Sobey C., Kondratiev V. I., Weltevrede P., Verbiest J. P. W., Karastergiou A., Kramer M., et al. 2015, A&A, 576, A62
- Osłowski S., van Straten W., Bailes M., Jameson A., Hobbs G., 2014, MNRAS, 441, 3148
- Petrova S. A., 2004, A&A, 424, 227
- Petrova S. A., 2008a, MNRAS, 384, L1
- Petrova S. A., 2008b, ApJ, 673, 400
- Rankin J. M., 1983, ApJ, 274, 333
- Rankin J. M., 1993, ApJ, 405, 285
- Rybicki G. B., Lightman A. P., 1979, Radiative processes in astrophysics. New York, Wiley-Interscience
- Seiradakis J. H., Gil J. A., Graham D. A., Jessner A., Kramer M., Malofeev V. M., Sieber W., Wielebinski R., 1995, A&AS, 111, 205
- Srostlik Z., Rankin J. M., 2005, MNRAS, 362, 1121
- Stinebring D. R., Cordes J. M., Rankin J. M., Weisberg J. M., Boriakoff V., 1984, ApJS, 55, 247
- Teixeira M. M., Rankin J. M., Wright G. A. E., Dyks J., 2016, MNRAS, 455, 3201
- Tiburzi C., Johnston S., Bailes M., Bates S. D., Bhat N. D. R., Burgay M., Burke-Spolaor S., Champion D., Coster P., D'Amico N., Keith M. J., Kramer M., Levin L., Milia S., Ng C., Possetti A., Stappers B. W., Thornton D., van Straten W., 2013, MNRAS, 436, 3557
- von Hoensbroech A., Xilouris K. M., 1997, A&AS, 126, 121
- Wang P. F., Wang C., Han J. L., 2015, MNRAS, 448, 771
- Weltevrede P., Stappers B. W., Edwards R. T., 2007, A&A, 469, 607
- Wright G. A. E., 2003, MNRAS, 344, 1041